Performance Analysis of Mass-Market GNSS Receivers in UAV Applications

Johann Diep
European Space Agency
Noordwijk, Netherlands
johann.diep@esa.int

David Gómez-Casco
European Space Agency
Noordwijk, Netherlands
david.gomez.casco@esa.int

Xurxo Otero Villamide
European Space Agency
HE Space Operations
Noordwijk, Netherlands
xurxo.otero@esa.int

Richard Dennis Swinden
European Space Agency
Noordwijk, Netherlands
richard.swinden@esa.int

Paolo Crosta
European Space Agency
Noordwijk, Netherlands
paolo.crosta@esa.int

***Abstract*—Unmanned aerial vehicles have become a crucial technology in a wide variety of fields. The availability and integrity of exact positioning feedback information are of paramount importance for the safety of many UAV applications. Global navigation satellite system receivers provide reliable and accurate positioning solutions in outdoor environments. However, they suffer strong performance degradation in harsher scenarios such as forests, urban canyons, or indoor environments. This paper addresses the performance of GNSS receivers installed on a drone. They were tested in different scenarios such as under open sky or in adverse conditions of signal reception. The solutions offered by the receivers were compared to RTK reference trajectories. Moreover, the advantage of including a stereo tracking camera in the setup to obtain a more accurate reference trajectory in some scenarios was analyzed. The results give insights on the accuracy and the quality of the measurements of current GNSS technologies in aerial applications.**

***Index Terms*—UAV, GNSS receivers, RTK reference, visual-inertial navigation, SLAM**

I. Introduction

Unmanned aerial vehicles (UAV) have gained more interests in the research and consumer community in recent years [2]. The global UAV market is growing rapidly nowadays and estimated to reach USD 25 billion by 2027 [3]. Thereby, these flying machines are widely used for civilian, commercial and military applications in areas such as industrial inspection [4], environmental mapping [5] or payload carrying [6]. In the latter case, Amazon Prime Air [7] is a noteworthy development, where Amazon uses a fleet of autonomous drones to deliver small-scale items. At a larger scale, Joby Aviation [8] acquired Uber Elevate, the former air taxi division of Uber, and is currently further developing their self-controlled heavy-duty electric vertical takeoff and landing (VTOL) aircrafts for the purpose of transporting human passengers. Especially in those autonomy use cases, the availability and integrity of exact positioning feedback information become essential for safety purposes.

In this context, global navigation satellite system (GNSS) [9] belongs to one of the most widely used method for navigating in outdoor environments. Consequently, there is a high interest for commercially available low-cost and light-weight GNSS receivers for applications in aerial maneuvers. Hence, the following publication describes the performance assessment of various GNSS technologies in different aeronautical drone flights.

Multiple GNSS behaviour analyses were conducted in the past for various use cases. Crosta et al. [10] evaluated the positioning accuracy of smartphones integrated with a commercially available dual frequency chip in multiple test campaigns. In particular, they tested those embedded mass-market receivers during static, walking and driving scenarios using custom pedestrian and vehicular setups. Their results compared against precise reference real-time kinematic (RTK) solutions showcased an improvement of dual frequency compared to single frequency in regards of positioning. However, they did not investigate the effect of high-dynamic movements on estimation accuracy since their experiments were all conducted at constant slow paces. Among others, we extend the type of used mobile setup in our work towards fast aerial applications.

In a previous publication by Mongrédien, Doyen, Strom and Ammann [11], receiver performance tests were conducted using an UAV in partially open-sky conditions. Their objective was to analyze the performance in scenarios with signal degradation due to environmental factors and the resulting impact on RTK positioning quality. In our work, the performances of several GNSS receivers in a wide variety of scenarios including open-sky, forest and indoor environments are compared. Additionally, the reactions of commercial receivers specifically

The European Space Agency (ESA) is an European intergovernmental organisation of 22 member states dedicated to the exploration and use of space for the benefit of humankind.

The work described in this paper was supported by the Commercial User Segment and Navigation System Validation (TEC-ESG) section [1] at the European Space Research and Technology Centre (ESTEC) as part of ESA in the Netherlands.

ESA provides the possibility for external European companies to use or loan the laboratory equipment (such as the UAV) for testing campaigns.

towards high acceleration aerial maneuvers and different flight heights are addressed.

Furthermore, an emphasis in this work was also put on the generation of high-quality reference trajectories, especially for traverses through obstructed areas. In those scenarios, RTK-based reference trajectories alone do not provide the required accuracy. Crosta et al. [10] indicated that additional low-grade sensors such as accelerometers, gyroscopes and magnetometers embedded for example in modern smartphones can further reduce the estimation errors. Their loosely-coupled inertial-GNSS integration approach showcases an increase in position and attitude awareness. Moreover, in the work by Siegwart and Nourbakhsh [12], the benefits of using visual sensors are introduced. In the standard visual odometry implementation, a rover-fixed camera is used to determine the relative position and orientation of the platform with respect to an initial state by processing the flow of features in sequential image frames. Instances of visual odometry, such as visual simultaneous localization and mapping (SLAM) [13], can achieve high accuracy for a medium-length trajectory. However, a drift, which increases over the traverse distance or time, can be observed while running. Moreover, in case of a monocular camera, the absolute scale of the position estimates is ambiguous. Lastly, distinct pixels within the current image, so-called features, are used by most algorithms for the processing step. Here, absence of features is less of an issue in dense metropolitan areas than it is in open texture-less environments. In contrast, satellite navigation provides absolute position estimations with the drawback of their accuracies being affected by environmental factors. While GNSS performs robustly in open-sky areas, it suffers from signal shadowing or multipath effects in urban areas in contrast. Hence, as showcased by Afia, Escher and Macabiau [14], a fusion between both navigation techniques can benefit from their respective complementary nature. In our drone setup, we were making use of a stereo tracking camera in order to additionally benefit from visual-inertial navigation information.

This paper describes the performance analysis of mass-market GNSS receivers in UAV applications. Thereby, an antenna, two GNSS receivers as well as a signal recorder were mounted on a drone. With the latter, the reactions of further receivers were generated in post processing. Additionally, the setup was also equipped with a commercial stereo tracking camera for additional visual-inertial odometry data. Furthermore, this publication shall also lay the foundation for our future publications which goes more into details on the topic.

The rest of the paper is organized as follows. Section 2 introduces the testing environments, the experimental drone setup with all its measurement components and the details on the generation of the reference trajectories. Section 3 provides the results and their findings. Lastly, a summary of the performance analysis with a short outlook can be found in section 4.

II. Method

Two testing campaigns in different environments (see Fig.1) with varying flight trajectories and parameters, hereafter called campaign 1 and 2, were conducted whereby the drone setup was modified slightly between them. Campaign 1 was conducted at the airport Twente in Enschede on the 17th of November 2020. Campaign 2 was conducted on the campus of ESTEC in Noordwijk on the 27th of July 2021. In the following, the experimental setup is explained in further detail.

A. Testing Environments

Fig. 1. The environments and the respective flight directions used for the performance analysis: (1) airport, (2) forest, (3) shelter, (4) football field, (5) tennis hall and (6) building corridor.

Campaign 1 included three testing environments with distinct objectives to analyse various influences on localization accuracy. The tests performed at the airport runway serve for the analysis of the influence of flight speed and elevation under open-sky. High-paced straight flight traverses were conducted at different heights respectively. Thereby, precise RTK reference data generated from the receiver measurements are fully available. The tests performed at the nearby forest serve for the analysis of the influence of sparse obstructions due the presence of canopies. Moderate-paced flight traverses at low height were conducted along a forest way. Here, RTK reference trajectories exhibit short gaps with no traverse information. Lastly, the tests performed at the nearby shelter serve for the analysis of the influence of complete obstructions due to concrete walls. Moderate-paced flight traverses at low height were conducted in an open shelter. Here, RTK reference trajectories exhibit large gaps with no traverse information.

Among others, campaign 2 contained two testing environments. The first test leads from the football field inside the tennis hall. While the first part serves for the analysis of the influence of flight speed under open-sky, the second part provides the scenario of complete obstructions due to closed space. At first, flight rounds along the football field

Fig. 2. The complete drone setup for the first test campaign: (1) GNSS antenna, (2) GNSS splitter, (3) 2 on-board receivers, (4) mini computer, (5) GNSS recorder and (6) external battery.

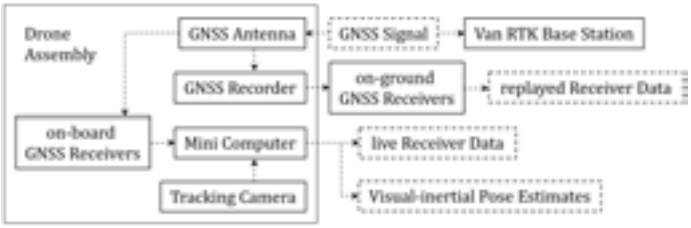

Fig. 3. Flowchart of the used hardware and their corresponding connections in order to generate the live and replayed receiver data. Furthermore, it showcases the tracking camera used to collect additional visual-inertial pose estimation information.

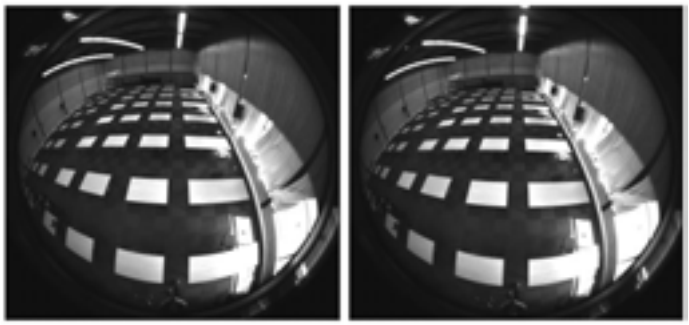

Fig. 4. An additional stereo tracking camera mounted on the bottom of the drone at a 45° downward angle was used for the second test campaign. It provides navigation information by combining visual SLAM with IMU measurements.

were conducted at different speeds. Thereafter, moderate-paced rounds were performed inside the tennis hall at different heights. While the part in open-sky contains fully available RTK information, the part within closed space exhibits large gaps with no RTK traverse data. The second test was performed around a building at moderate speed. The objective is to analyse the influence of lateral obstructions due to the building walls. Here, RTK reference data are fully available. Furthermore, both tests serve to evaluate the utility of the additional tracking camera towards seamless indoor/outdoor localization and hence a possible improvement in reference quality.

B. On-board GNSS Receivers and Recorder

As described in the following subsection II-C, in this performance analysis, the drone setup included two identical on-board mass-market GNSS receivers (hereafter called Live RX1 with its individual configuration), which are capable of tracking all global civil navigation systems, for the collection of live data.

The Spirent GSS6450 multi-frequency recorder [15] stores the GNSS signals received by an antenna in digital form. Hence, replayed data from various mass-market receivers of different manufacturers (hereafter called Replay RX1, RX2 and RX3 with their individual configuration) were generated in post processing by feeding them the stored digital signals and saving the corresponding responses. Furthermore, a sample check with the on-board receiver demonstrated high resemblance between the replayed and the live responses. This method is of advantage since it allows for keeping the number of on-board receivers to a minimum and consequently reduces the overall weight of the payload. Thereby, in the context of this paper, the performances of two further receivers were evaluated.

C. Drone Assembly

The experiments were carried out on the Matrice 600 drone [16]. It is a heavy duty radio-controlled hexacopter made by Da-Jiang Innovations (DJI) which uses six body-fixed rotor blades to create lift for maneuver, vertical take-off and landing. Without additional payload, it can reach a speed of 18 m/s. The maximum takeoff weight is 15.1 kg.

Fig. 2 illustrates the assembly of the drone with all its payload attached on custom holders under the rotor wings and Fig. 3 showcases the corresponding flowchart of the used hardware and their connections in order to generate the live and replayed receiver data as well as the visual-inertial pose estimates. The GNSS antenna was attached above the wings in order to maximize signal reception. The Tallysman TW7972 antenna [17] was used for campaign 1, which covers GPS/QZSS L1/L2/L5, GLONASS G1/G2/G3, Galileo E1/E5a/E5b and BeiDou B1/B2/B2a. For campaign 2, the Tallysman VSM6028L antenna [18] was used, which additionally covers QZSS L6, Galileo E6 and BeiDou B3. The antenna was connected to a GNSS splitter which distributes the received signal to the GNSS recorder as well as the two on-board receivers. The data from the latter were collected by an Intel NUC7i7DNHE mini computer [19]. It is noted that the two receivers were configured to track different signals. One was using GPS L1/L5, GLONASS L1, BeiDou B1/B2a and Galileo E1/E5a (hereafter called configuration 1), the other GPS L1/L2, GLONASS L1/L2, Beidou B1/B2I and Galileo E1/E5b (hereafter called configuration 2). Additional external batteries were carried on-board in order to provide the power for the GNSS recorder as well as the mini computer.

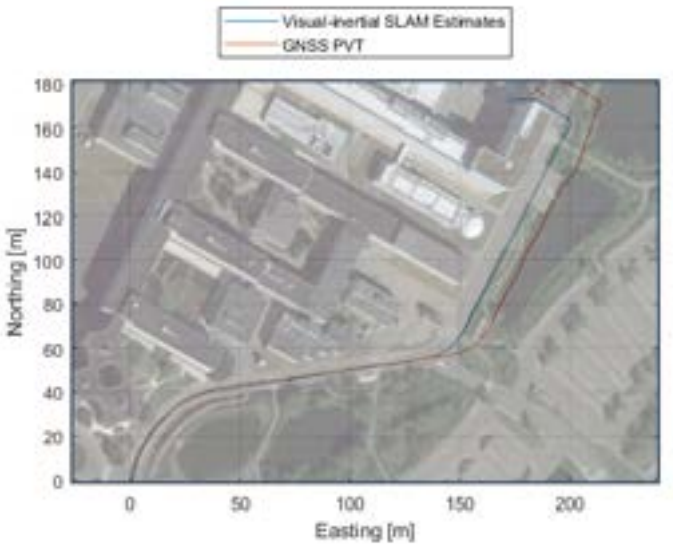

Fig. 5. Comparison of visual-inertial SLAM and GNSS during a walking test at the ESTEC campus. A 200 meters long path along the middle of the road was followed while holding the camera and GNSS setup.

D. On-board Tracking Camera

For campaign 2, an Intel Realsense tracking camera T265 [20] was used for additional visual-inertial navigation data (see Fig. 4). It consists of two fisheye lens sensors, a built-in inertial measurement unit (IMU) as well as a vision processing unit (VPU). All estimation algorithms run directly on the VPU and are made available through its driver, which stores the data in a robot operating system (ROS) compatible format. An additional ROS subscriber package written in C++ was created in order to parse them into the desired format for analysis. Some pedestrian-based reliability tests showcase its ability to estimate the correct scales and shapes of traverses (see Fig. 5). Furthermore, under well illuminated conditions, the sensor provided an average closed-loop error of around 2 meters after traverses which are greater than 120 meters in length. The sensor was mounted on the bottom of the drone at a 45° downward angle in order to have a balanced amount of fast-moving features on the ground and static features on the horizon.

E. Reference Trajectory

The estimated trajectory are compared against the RTK reference trajectories which are generated using Inertial Explorer [21]. Here, the ESA van [22] in open-space and the ESTEC navigation facility [23] were used as base stations for campaign 1 and 2 respectively in order to generate precise RTK references. Furthermore, multiple estimations of RTK based on various receivers were compared against each other as well as with the DJI on-board GNSS log files[1]. Thereby, the

[1]It is noted that the DJI flight recorder of the Matrice 600 drone uses the on-board barometer sensor to obtain height information. They are not highly accurate and degrade the overall 3D positioning accuracy when combined with the GNSS-sourced horizontal position data in the log.

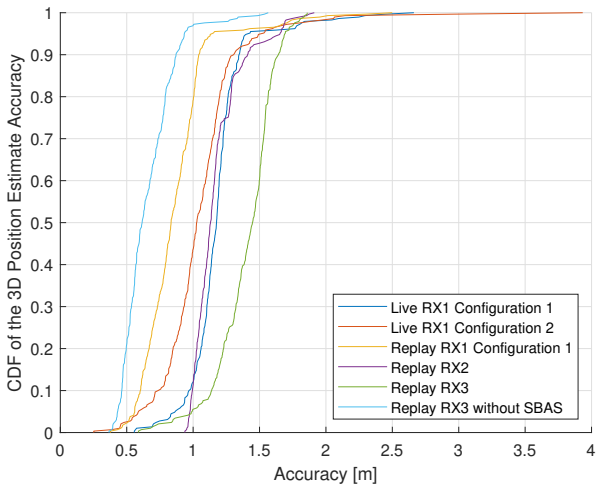

Fig. 6. CDF of the 3D position estimate accuracy of the airport traverse at 5 meters flight height.

different RTK solutions showcased minimal differences in the open-sky traverses. For the performance analysis in section III, RTK references calculated based on the live on-board receiver data with configuration 1 were chosen for referencing.

F. Scope of this Paper

Within the scope of this paper, all receiver data from campaign 1 were assessed. In contrast, the open-sky and indoor traverse on the football field and tennis hall respectively as well as the open-sky traverse around the building from campaign 2 were used solely to evaluate the performance of the collected visual-inertial estimations against RTK solutions. The complete evaluation of all GNSS data of test campaign 2, which contains further large-scale traverses collected in an open field close to Voorhout, will be part of a future publication.

III. Results and Discussion

Human-controlled and autonomous hexacopter flight experiments were conducted at the testing environments described in subsection II-A to evaluate the performance of the mentioned receivers from subsection II-B. All the results and their corresponding interpretations are presented in this section. Designated Matlab scripts were used in order to produce the position estimates from the live and the replayed responses. In the process, the satellite ephemeris data at the time of the test campaigns is needed, which can be downloaded from Celestrak (https://www.celestrak.com/).

A. Airport Results

The first traverse was conducted at the airport at 5 meters flight height. The drone flew straight forward and back along a 300 meters long section of the runway.

As illustrated in the cumulative distribution function (CDF) plot in Fig 6, the 95-percentile 3D-errors of all receivers are within the interval 0.9 to 1.7 meters. It is noted that

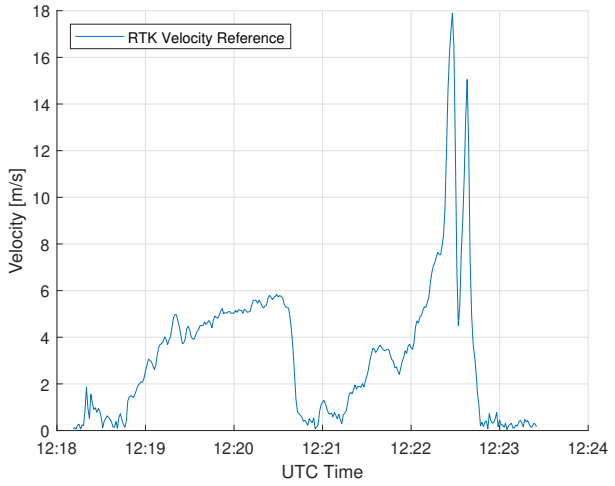

Fig. 7. RTK velocity plot of the airport traverse at 5 meters flight height.

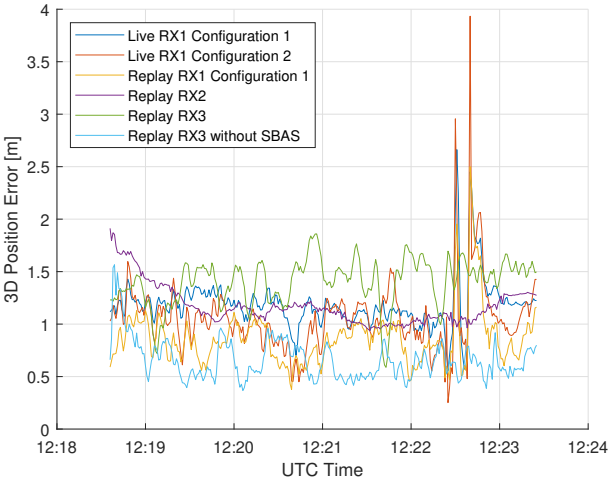

Fig. 8. 3D position error plot of the airport traverse at 5 meters flight height.

the satellite-based augmentation system (SBAS) corrections contribute heavily towards a bias in the position estimation of the RX3 receiver, which seems to indicate that the receiver is not optimized for SBAS usage. Fig. 7 illustrates the velocity estimates based on RTK. As can be seen, the flight velocity was slowly increased along the track. Thereby, it reaches a peak value of 18 m/s during the return flight. As can be seen in Fig. 8, this coincides with a rise in 3D position estimate errors of both live on-board RX1 receivers with configuration 1 and 2 respectively as well as the replayed RX1 receiver with configuration 1. Therefore, one can conclude that the RX1 receiver is sensitive towards high-dynamic motions which include fast accelerations. RX2 showcases a relative high 95-percentile error of 1.66 meters. However, it was revealed that this bias stems mainly from erroneous height estimations. An exclusion of the height component revealed a much lower 95-percentile horizontal error of around 0.6

TABLE I
ERROR IN THE FOREST AND SHELTER TRAVERSE

	95-Percentile 3D Error [m]	
Receiver	Forest	Shelter
Live RX1 Configuration 1	5.435	24.118
Live RX1 Configuration 2	5.179	25.699
Replay RX1 Configuration 1	5.439	32.249
Replay RX2	9.16	35.95
Replay RX3	5.999	30.084
Replay RX3 without SBAS	6.713	38.178

meters, which suggests that this receiver uses techniques to prioritise horizontal over vertical positioning accuracy. Similar characteristics can be observed for the flights conducted at different heights up to 100 meters which indicates that flight height does not have a major impact on receiver behaviour.

B. Forest and Shelter Results

In instances of the forest and shelter traverses, an increase in 95-percentile 3D-error can be observed (see Table I) in comparison with the previous discussed performance of the airport traverse (see subsection III-A). Due to the degree of obstructions present in those scenarios, the degradations are expected from a quantitative standpoint. However, the sparsity of reference trajectories as elaborated in subsection II-A makes qualitative analysis unfeasible. Furthermore, comparisons of available RTK data computed with two receivers exhibit large differences for both scenarios, which indicate that the available reference information is not reliable enough. Those findings are expected since GNSS is affected by environmental factors. While it performs robustly in the open-sky airport traverses, it suffers from signal shadowing or multipath effects due to the forest canopies and shelter in contrast.

C. Observables Analysis

In order to further evaluate the differences between the airport, forest and shelter scenarios, a comparison of the respective GNSS observables obtained through the RX3 receiver was conducted. Specifically, the carrier-to-noise ratios $\mathrm{CN}_{0,i}$ were contrasted against the respective code noises N_i. As described by Pirazzi, Mazzoni, Biagi and Crespi [24], the latter can be determined by taking the third derivative of the code measurements and factoring in $1/\sqrt{20}$ as a normalization constant as follows (see 1) where R_i corresponds to the pseudorange measurement at the time instant i:

$$N_i = \frac{1}{\sqrt{20}} \cdot \left(R_{i+3} - 3 \cdot R_{i+2} + 3 \cdot R_{i+1} - R_i \right) \quad (1)$$

In the following analysis, only signals from global positioning system (GPS) with the L1 carrier frequency are considered as a benchmark. Fig. 9 illustrates datapoints from the respective environments. Each datapoint represents a signal

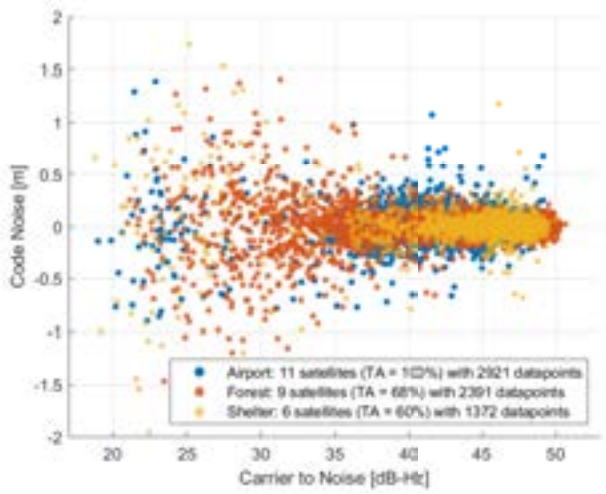

Fig. 9. Comparison of carrier-to-noise ratio versus code noise for the signals gathered in the airport, forest and shelter environments.

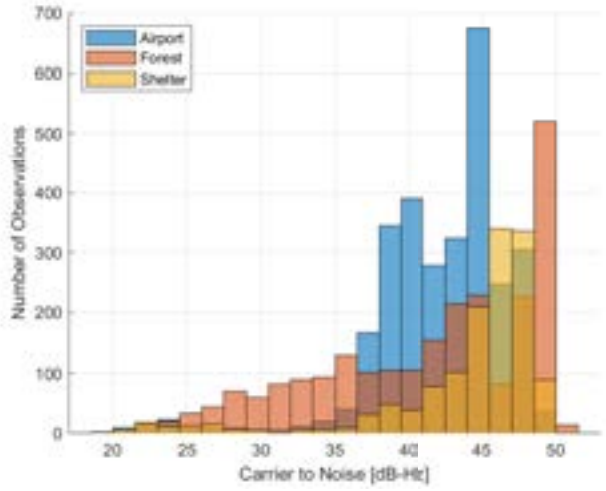

Fig. 10. Histogram of the carrier-to-noise ratio for the traverses at the airport, forest and shelter environments.

sent by a specific GPS satellite which was visible during the time period of the flight. Thereby, the color represents the specific environment where the signals were collected. In order to allow for an unbiased comparison, only the data collected during a 5 minutes time window in each traverse scenario were considered.

As expected, the number of visible satellites decreases going from open-sky to more obstructed scenes. A total of 11 satellites were in range at the airport runway, 9 satellites were visible in the forest and only 6 satellites were prominent at the shelter traverse. Consequently, an increased exposure to satellites leads to greater number of signal receptions and therefore more datapoints. It is also noted that as described in subsection III-B, the tracking availability (TA) decreases with an increase in the degree of obstructions. As can be seen, the forest traverse contains a wider spread of datapoints across the

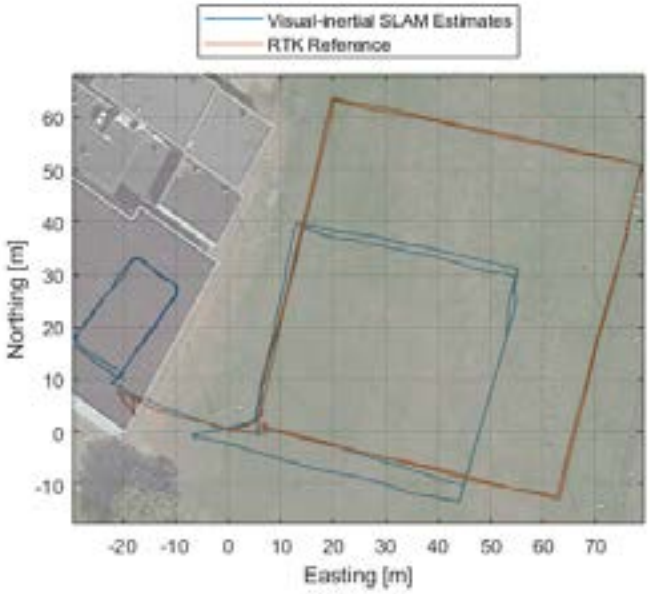

Fig. 11. Comparison of visual-inertial position estimates with RTK reference for the football field and tennis hall traverse.

CN_0 spectrum, whereas lower CN_0 values are observed to have high code noises. This is expected since the forest canopies contributes heavily towards signal refraction. In contrast, a big part of the datapoints from the airport traverse are located at higher CN_0 values with lower code noise values. Furthermore analysis showcased that the few datapoints located between 20-30 dB-Hz belong to two satellites with low elevation, which therefore contribute to higher code noises. The same two satellites also contributes to the large code noise outliers at higher CN_0. As for the shelter traverse, signal tracking was lost completely once the drone enters the covered shelter. Hence, only measurements during the part of the traverse in open-sky are available. This phenomena can also be observed in Fig. 10, where the distribution of the CN_0 values is illustrated. The peaks of the CN_0 values for each scenario are contributed through exposure to open-sky in the respective traverse. Thereby the differences in the locations of the peaks between the airport, forest and shelter scenarios are due to temporal differences of the experiments and the consequent distinctions in satellite constellation geometries.

D. Tracking Camera Reliability Test

Two on-board reliability tests with the tracking camera were conducted during test campaign 2. The objective is to get a feeling of the reliability of the collected visual-inertial SLAM navigation data in comparison with RTK. As can be seen in Fig. 12, the tracking camera was able to estimate the scale and shape of the flight traverse initially. The final error after traveling a distance of 140 meters is around 10 meters, which is greater than what we expected from previous tests. The relative large deviation from the reference trajectory on the east side of the traverse most likely stems from the expected

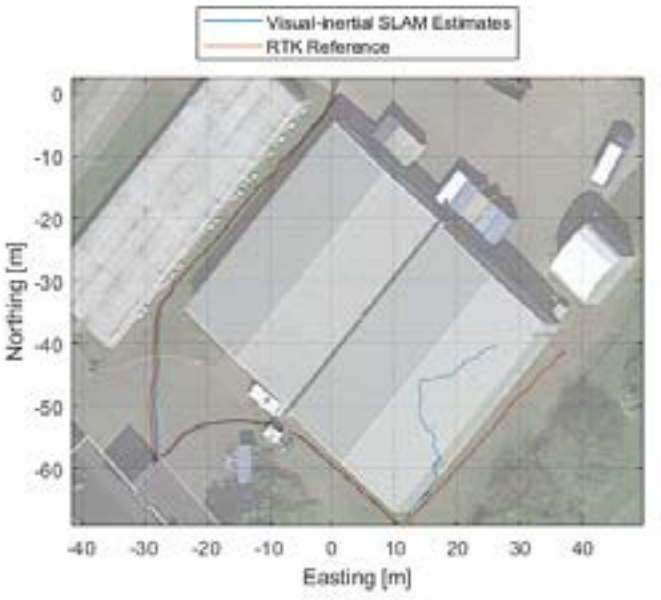

Fig. 12. Comparison of visual-inertial position estimates with RTK reference for the building corridor traverse.

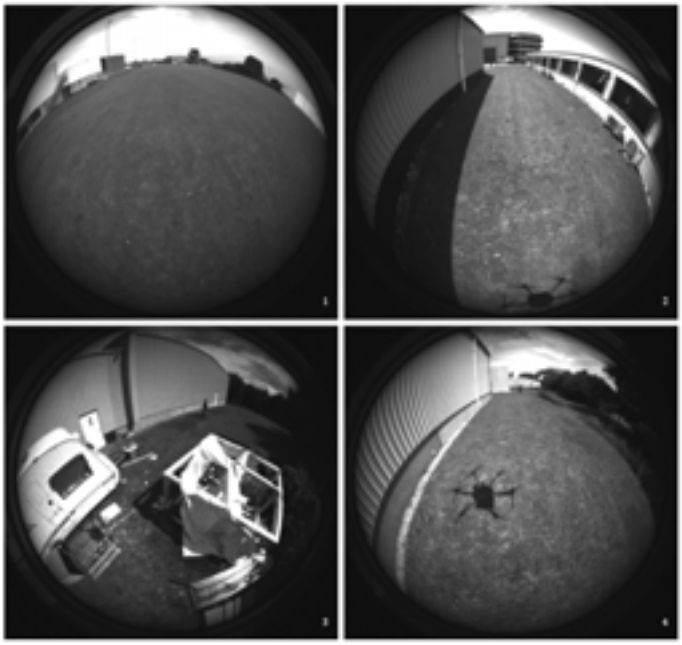

Fig. 13. Comparison of the sceneries of the two traverses during campaign 2: (1) football field as well as the (2) west, (3) south and (4) east part of the building corridor.

drift away from the RTK solution due to error propagation after the initial track, but can also be caused by the lack of distinct features near the ground. As can be seen in Fig. 13, the west side of the traverse offers recognizable features on the window corners to the right edge of the image. The obstacles on the south side also provide valuable information for movement estimation. However, the east side presents very little distinct features on the textureless ground, which leads to a higher divergence from the reference. It is noted that in case of the building corridor scenario this error is calculated based on the RTK reference, which by itself may contains errors due to signal refraction caused by the nearby walls. The same effect of lack of distinct features in the scenery can also cause the difference in trajectory scale between the SLAM and the RTK during the football field traverse as shown in Fig. 11 and Fig. 13. However, after the first round, the SLAM was able to regenerate from the drift. As explained in a publication by Hausamann, Sinnott, Daumer and MacNeilage [25], this effect stems from the re-localization of the device due to loop closure, which corrects the current estimate of the pose based on the re-observation of previously observed features. However, in contrast to i.a. ORB-SLAM [26], it seems that this re-localization only corrects the current pose while previous poses are unaffected. Furthermore, it can be seen that the tracking camera, in contrast to GNSS, still provide data during the part of the traverse within the tennis hall. Therefore, despite its drawbacks, the ability to track the traverse without external sensors makes visual-inertial odometry a valuable source of reference information for future performance analysis in obstructed scenarios.

IV. Conclusion

This publication deals with the performance analysis of mass-market GNSS receivers in UAV applications. This section summarises its findings and gives an outlook on future publications.

A. Findings

Multiple receivers were evaluated during aerial maneuvers in multiple scenarios which include an open-sky airport runway and obstructed areas like a forest walkway and a shelter. The first tests at the airport runway were conducted at various heights, where similar results can be found. During the open-sky traverses at the runway, all receivers performed similarly with a average 95-percentile 3D position estimation error of around 0.9-1.7 meters at low flight velocity up to 6 m/s. At high-velocity motions up to 18 m/s, both on-board receivers as well as their replayed counterpart showcased significant worse position, velocity and time (PVT) estimation solutions.

As for the forest and shelter traverse, no performance analysis was made due to unreliable reference information caused by various GNSS effects in obstructed scenarios. A comparison of the observables from each scenario gave some further insights. Most satellites were visible in the open-sky airport traverse. Thereby, most received signals had high CN_0 values with low code noises. In comparison, due to signal refraction, fading or reflection effects, the forest traverse had a greater number of signals at the lower CN_0 spectrum with a higher code noises. The shelter traverse had the least amount of received signals due to the fact that the receiver lost tracking once the UAV entered the shelter. In the latter case,

all measured signals were collected in open-sky shortly before entering the closed space.

Lastly, the visual-inertial navigation data from the tracking camera were compared against RTK solutions. Thereby, they showcased the ability to track the scale and shape of the flight trajectories. Due to error-propagation, the average drift after a 110 meters flight is around 2 meters, which is within the usual fault tolerance of standard visual odometry algorithms. Hence, the additional tracking camera sensor is a valuable asset for future reference information.

B. Future Work

During test campaign 2, further large-scale traverses with controlled velocities were performed. It is therefore interesting to investigate if the phenomena of higher PVT error at high-velocity reoccurs. Furthermore, different kinds of high-dynamic maneuvers were conducted such as rapid elevation changes or yawing in order to investigate potential correlation with PVT errors. A higher number of mass-market and professional receivers were tested during the second campaign. This shall give broader insights on their general behaviour in UAV applications. Lastly, it is to be investigated if sensor fusion of data coming from the tracking camera and raw GNSS measurements in a tightly-coupled approach would increase the reference reliability.

V. Disclaimer

This research project was conducted as part of the Young Graduate Trainee (YGT) program by the first author. In case of further inquiry, he can also be reached under his private e-mail address (johanndiep@gmail.com) as well. The content of the present article reflects solely the authors' view and by no means represents the official ESA or GALILEO views.

Acknowledgment

Aspects of this publication were only possible due to the continuous ESA internal and external support we received. A special thanks goes to Gerarda Depasquale for helping us generating the RTK solutions for our analysis. Furthermore, we would like to thank Jurgen van Ooijen for helping us finding the test locations at the ESTEC campus. Lastly, our gratitude also goes to the people from Customdrone, Space53 and Zero Gravity Drone for supporting us with the deployment of our UAV during the test campaigns.

References

[1] European Space Agency, "Commercial user segment and navigation system validation," https://www.esa.int/Enabling_Support/Space_Engineering_Technology/Radio_Frequency_Systems/Navigation_Laboratory_NavLab, 2021, accessed: 2021-11-04.

[2] I. H. Beloev, "A review on current and emerging application possibilities for unmanned aerial vehicles," *Acta technologica agriculturae*, vol. 19, no. 3, pp. 70–76, 2016.

[3] Fortune Business Insights, "Unmanned aerial vehicle market," https://www.fortunebusinessinsights.com/industry-reports/unmanned-aerial-vehicle-uav-market-101603, 2020, accessed: 2021-10-22.

[4] J. Nikolic, M. Burri, J. Rehder, S. Leutenegger, C. Huerzeler, and R. Siegwart, "A uav system for inspection of industrial facilities," in *2013 IEEE Aerospace Conference*, 2013, pp. 1–8.

[5] F. Nex and F. Remondino, "Uav for 3d mapping applications: a review," *Applied Geomatics*, vol. 6, no. 1, p. 1–15, 2013.

[6] J. A. Benito, G. Glez-de Rivera, J. Garrido, and R. Ponticelli, "Design considerations of a small uav platform carrying medium payloads," in *Design of Circuits and Integrated Systems*, 2014, pp. 1–6.

[7] Amazon, "Amazon prime air," https://www.amazon.com/Amazon-Prime-Air/b?ie=UTF8\&node=8037720011, 2021, accessed: 2021-10-25.

[8] Joby Aviation, "Joby aviation," https://www.jobyaviation.com/, 2021, accessed: 2021-10-25.

[9] P. D. Groves, *Principles of GNSS, inertial, and multisensor integrated navigation systems*. Artech House, 2013.

[10] P. Crosta, G. Galluzzo, R. L. Rodriguez, X. Otero, P. Zoccarato, G. De Pasquale and A. Melara, "Galileo hits the spot," https://insidegnss.com/galileo-hits-the-spot/, 2019, accessed: 2021-10-22.

[11] C. Mongrédien, J.-P. Doyen, M. Strom, and D. Ammann, "Centimeter-level positioning for uavs and other mass-market applications," in *Proceedings of the 29th International Technical Meeting of the Satellite Division of The Institute of Navigation (ION GNSS+ 2016)*, Portland, Oregon, September 2016, pp. 1441–1454.

[12] R. Y. Siegwart and I. R. Nourbakhsh, *Introduction to autonomous mobile robots*. MIT, 2004.

[13] C. Cadena, L. Carlone, H. Carrillo, Y. Latif, D. Scaramuzza, J. Neira, I. Reid, and J. J. Leonard, "Past, present, and future of simultaneous localization and mapping: Toward the robust-perception age," *IEEE Transactions on Robotics*, vol. 32, no. 6, pp. 1309–1332, 2016.

[14] A. B. Afia, A.-C. Escher, and C. Macabiau, "A low-cost gnss/imu/visual monoslam/wss integration based on federated kalman filtering for navigation in urban environments," in *Proceedings of the 28th International Technical Meeting of the Satellite Division of The Institute of Navigation (ION GNSS+ 2015)*, Tampa, Florida, September 2015, pp. 618–628.

[15] Spirent, "Gss6450 record and playback system specifications," https://www.spirent.com/products/gnss-rf-record-and-playback-system-gss6450\#overview, 2021, accessed: 2021-10-26.

[16] DJI, "Matrice 600 specifications," https://www.dji.com/nl/matrice600/info, 2021, accessed: 2021-10-25.

[17] Tallysman, "Tw7972 antenna specifications," https://www.tallysman.com/product/tw7972-triple-band-gnss-antenna-with-l-band/, 2021, accessed: 2021-10-26.

[18] ——, "Vsm6028l antenna specifications," https://www.tallysman.com/product/vsm6028l-embedded-verostar-full-gnss-precision-antenna-l-band/, 2021, accessed: 2021-10-26.

[19] Novatel, "Inertial explorer," https://novatel.com/products/waypoint-post-processing-software/inertial-explorer, 2021, accessed: 2021-10-27.

[20] Intel, "Realsense tracking camera t265 specifications," https://www.intelrealsense.com/tracking-camera-t265/, 2021, accessed: 2021-10-26.

[21] ——, "Nuc7i7dnhe mini computer specifications," https://ark.intel.com/content/www/us/en/ark/products/130393/intel-nuc-kit-nuc7i7dnhe.html, 2021, accessed: 2021-10-26.

[22] E. Breeuwer, S. Binda, G. Lopez-Risueno, D. Blonski, A. Mudrak, F. Gonzalez, R. Prieto-Cerdeira, I. Stojkovic, J. Hahn, M. Falcone, "Galileo works!" https://insidegnss.com/wp-content/uploads/2018/01/marapr14-Galileo-Works.pdf, 2014, accessed: 2021-10-28.

[23] G. Galluzzo, R. L. Rodriguez, R. Morgan-Owen, D. B. S. Binda, P. Crosta, F. Gonzalez, J. M. Garcia, X. Otero, N. Sirikan, M. Spangenberg, E. Spinelli, R. Swinden, and S. Wallner, "Galileo system status, performance metrics and results," in *Proceedings of the 2018 International Technical Meeting of The Institute of Navigation*, Reston, Virginia, January 2018, pp. 790–809.

[24] G. Pirazzi, A. Mazzoni, L. Biagi, and M. Crespi, "Preliminary performance analysis with a gps+galileo enabled chipset embedded in a smartphone," in *Proceedings of the 30th International Technical Meeting of the Satellite Division of The Institute of Navigation (ION GNSS+ 2017)*, Portland, Oregon, September 2017, pp. 101–115.

[25] P. Hausamann, C. B. Sinnott, M. Daumer, and P. R. Macneilage, "Evaluation of the intel realsense t265 for tracking natural human head motion," *Scientific Reports*, vol. 11, no. 1, 2021.

[26] R. Mur-Artal, J. M. M. Montiel, and J. D. Tardos, "Orb-slam: A versatile and accurate monocular slam system," *IEEE Transactions on Robotics*, vol. 31, no. 5, p. 1147–1163, 2015.